Boron doped BiOBr nanosheets with enhanced photocatalytic inactivation of *Escherichia coli*

Dan Wu,[a] Songtao Yue,[b] Wei Wang,[b] Taicheng An,[c,*] Guiying Li,[d] Ho Yin Yip,[a] Huijun Zhao,[e] Po Keung Wong[a,*]

[a] School of Life Sciences, The Chinese University of Hong Kong, Shatin, NT, Hong Kong SAR, China

[b] College of Materials Science and Engineering, Huazhong University of Science and Technology, Wuhan 430074, China

[c] State Key Laboratory of Organic Geochemistry, Guangzhou Institute of Geochemistry, Chinese Academy of Sciences, Guangzhou 510640, China

[d] Institute of Environmental Health and Pollution Control, School of Environmental Science and Engineering, Guangdong University of Technology, Guangzhou 510006, China.

[e] Centre for Clean Environment and Energy, Gold Coast Campus, Griffith University, Queensland 4222, Australia

*Corresponding authors:

Taicheng An: Tel: +86 20-8529-1501, Fax: +86 20-8529-0706, E-mail: antc99@gig.ac.cn; Po Keung Wong: Tel: +852 3943-6383, Fax: +852-2603-5767, E-mail: pkwong@cuhk.edu.hk.

Abstract

Boron (B) doped bismuth oxybromide (B-BiOBr) nanosheets were synthesized using a hydrothermal method and their photocatalytic activities were investigated through inactivating a typical bacterium, *Escherichia coli* K-12 using fluorescence tubes as visible light (VL) sources. B atoms are successfully doped into the crystal lattice of BiOBr. However, the morphology, crystal structure, and {001}-facet exposed feature of B-BiOBr nanosheets remain unchanged compared with pure BiOBr nanosheets. Significantly, the as-prepared B-BiOBr nanosheets show superior activity in the photocatalytic inactivation of *E. coli* K-12 over pure BiOBr nanosheets under VL irradiation. Photogenerated h^+ is evidenced to be the major reactive species accounting for the inactivation process of B-BiOBr. With its electron-deficient characteristics, the B dopant is favorable to accept extra e^- from VB of BiOBr, leading to improved charge carrier separation efficiency. The greatly enhanced bacterial inactivation efficiency was attributed to the synergic advantages of enhanced VL adsorption capability and more amount of photogenerated h^+ with higher oxidative ability. In addition, the destruction process of bacterial cell was also observed from the destruction of cell membrane to the intracellular components.

Keywords

Visible-light-driven photocatalyst; BiOBr nanosheet; Boron doping; Photocatalytic inactivation; *Escherichia coli*

1. Introduction

Photocatalysis is accepted to be a promising technology for microbial disinfection in terms of utilizing either the sustainable solar energy or artificial indoor light [1-4]. Nevertheless, most of the widely studied semiconductor photocatalysts, such as TiO_2 and ZnO, process wide band gap and thus limit their photo-absorption to UV region, which hinder their practical energy utilization [5-7]. Therefore, the development of visible-light-driven (VLD) photocatalysts has been a growing concern. Bismuth oxybromide (BiOBr), as an important V-VI-VII ternary semiconductor, has recently drawn great attention due to its fascinating physicochemical prosperities, suitable bandgap, good VLD photocatalytic activity and high chemical stability, which are originated from its unique layered structure [8, 9]. BiOBr has a tetragonal structure consisting of $[Bi_2O_2]$ slices interleaved by double slabs of Br atoms. This asymmetric decahedral crystal structure with strong intra-layer covalent bonding and weak inter-layer van der Waals interaction endows BiOBr with various applications in the photocatalytic environmental purification [10-13]. Therefore, it is of great significance to extend BiOBr photocatalysis in microbial inactivation, which is one of the key subjects of environmental purification.

Although BiOBr exhibits excellent photocatalytic activity under visible light (VL) irradiation, the overall photocatalytic efficiency is still comparatively low, thus limiting its practical applications. To attempt efficiently harvest solar energy, it is indeed of great importance to modulate BiOBr nanosheets to acquire better VLD photocatalytic performance. Among various modification strategies, metallic (such as Fe [14], Al [15], Mn [16], Ag and Ti [17]) or non-metallic (such as I [18], C [11], N and S [19]) heteroatom doping is one of the

most successful approaches to increase the VL response of BiOBr photocatalyst. However, metallic dopants still suffer from multiple drawbacks, such as susceptibility to environment, photocorrosion of dopants, and limited natural reserves [20, 21]. In this respect, as an intensively investigated dopant, boron (B) has emerged as an ideal nonmetallic candidate to be accommodated and diffused within semiconductor lattice owing to its fascinating physicochemical properties (light weight, high chemical resistance and typical semi-conductivity) [22]. Comparing with the aforementioned nonmetallic ions, B has smallest ion radius (0.023 nm), so that it can be easily incorporated into the crystal framework of semiconductors [23]. Additionally, as the source of B, boric acid is environmentally compatible, cheap, easy to handle, and already widely used in industrial processes [24]. In particular, the electron configuration of B leaves one empty *p*-orbital and renders B electron-deficient [25]. Therefore, the chemical environment around each B atom is thus dominated by its electron-deficient character [25, 26], which is expected to facilitate charge separation in the photocatalysis. Besides, some photocatalysts in pioneering work, such as TiO_2 [27], Bi_2WO_6 [28] and $BiVO_4$ [29], exhibited enhanced photocatalytic activity after B doping. Inspired by these advantages of B, modification of BiOBr with B dopants is expected to open up new possibilities for the enhancement of its photocatalytic performance. However, to the best of our knowledge, relative work has not been reported so far regarding a B-doped BiOBr photocatalyst as well as concerning its VLD photocatalytic bacterial inactivation activity.

Herein, in this work, B-doped BiOBr (B-BiOBr) nanosheets were first successfully synthesized through a facile hydrothermal method using boric acid as a B source. The

application of B-BiOBr in photocatalysis was assessed by inactivating a model bacterium, *Escherichia coli* K-12 using fluorescence tubes (FT) as VL sources. The effects of B doping on the intrinsic characteristics of BiOBr crystals were investigated in detail. Furthermore, the mechanism of improved photocatalytic bacterial inactivation activity of B-BiOBr is also proposed accordingly.

2. Experimental

2.1. Photocatalyst synthesis

B doped BiOBr nanosheets were prepared via a facile hydrothermal method. Typically, 4 mmol $Bi(NO_3)_3 \cdot 5H_2O$ and 0.03 mmol H_3BO_3 (molar ratio of B/Bi = 0.75%) were dissolved in 15 mL HNO_3 aqueous solution (0.7 M) under stirring. Then 50 mL KBr aqueous solution (0.01 M) was added into the above solution followed by stirring for 0.5 h at room temperature. The resultant was subsequently transferred into a 100 mL Teflon-sealed autoclave and heated at 160 °C for 12 h. After cooling to the room temperature, the precipitate was centrifuged, washed with distilled (DI) water for several times, and finally dried at 60 °C in an oven. Samples with B/Bi molar ratio of 0.25%, 0.5% and 1% are also prepared for comparison. The obtained products was accordingly denoted as 0.25B-BiOBr, 0.5B-BiOBr, 0.75B-BiOBr, and 1B-BiOBr, respectively. Pure BiOBr nanosheets were also prepared under the same conditions without boron doped. All the chemicals used in the experiments were of reagent grade and used as received without further purification.

2.2 Photocatalyst characterizations

The X-ray diffraction (XRD) patterns of as-prepared samples were measured by a SmartLab X-ray diffractometer (Rigaku, Japan) operating at 40 mA and 40 kV with Cu Kα as radiation source. Morphology of samples was observed using a Sirion 200 field-emission scanning electron microscope (SEM) (FEI, Netherlands) equipped with an energy-dispersive X-ray spectrometer (EDS) (EDAX Inc., USA) and Tecnai F20 high resolution TEM (HRTEM) (FEI, Hillsboro, USA). The X-ray photoelectron spectroscopy (XPS) analysis was performed by an AXIS-ULTRA DLD-600W spectrometer (Shimadzu–Kratos, Japan). UV-vis diffuse reflectance spectra (DRS) of samples were recorded with a Varian Cary 500 UV-vis spectrophotometer (Palo Alto, USA) equipped with a Labsphere diffuse reflectance accessory. The Raman spectra of samples were measured using a LabRAM HR800 Raman spectrometer (Horiba JobinYvon, France) with the excitation of a 532 nm laser beam. The Brunauer-Emmett-Teller (BET) specific surface area was measured by an ASAP 2020 volumetric adsorption analyzer (Micromeritics, USA). Electron paramagnetic resonance (EPR) spectra were recorded on a Bruker EMX EPR spectrometer equipped with a variable temperature helium flow cryostat system (Oxford Instruments, UK). Concentration of potassium ions was determined by a Z-2700 atomic absorption spectrophotometer (AAS) (Hitachi, Japan).

2.3 Mott–Schottky plot

The Mott–Schottky plots were conducted by using a CHI 660D electrochemical workstation (Shanghai Chen Hua Instrument Company, China) in a three-electrode cell with a Pt plate and a saturated Ag/AgCl electrode respectively as counter electrode and reference

electrode. 5 mg of the as-prepared photocatalyst and 15 μL of Nafion@ 117 solution (5 wt%) were dispersed in a 1 mL water/isopropanol mixed solvent (3:1 v/v) by sonication to form a homogeneous colloid. Subsequently, 0.1 mL of the colloid was deposited onto the fluorine doped tin oxide (FTO) glass with an area of about 1 cm^2). Prior to measurement, the working electrodes were immersed in Na_2SO_4 solution (0.1 M) for 30 s. The applied potential ranged from −1.0 to 0.5 V (*vs.* Ag/AgCl) with a frequency of 2 kHz.

2.4 Bacteria preparation

The bacterial strain of *E. coli* K-12 was inoculated into 50 mL of Nutrient Broth (Lab M, Lancashire, UK) and incubated at 37 °C for 16 h in a shaking incubator. The bacterial cells were harvested by the centrifugation of 1 min in an Eppendorf tube by a Z323 microcentrifuge (Hermle Labortechnik GmbH, Wehingen, Germany), then washed twice with sterilized DI water, and finally resuspended in sterilized DI water. The final cell density was adjusted to about 1×10^7 colony forming unit (CFU) mL^{-1}.

2.5 Photocatalytic bacterial inactivation

The VLD photocatalytic inactivation of *E. coli* K-12 by B-BiOBr nanosheets was conducted under fluorescent tubes (FT, 15 W, FSL, Foshan, China) irradiation. A suspension (50 mL) containing the bacterial cells and the photocatalyst (50 mg) in a flask was placed in dark under continuous stirring for 0.5 h to reach the adsorption equilibrium. Then the FT was turned on to start the photocatalytic inactivation experiments. At different time intervals, aliquots of the samples were collected and serially diluted with sterilized aqueous solution. Then 0.1 mL of the diluted samples was immediately spread on Nutrient Agar (Lab M, Lancashire, UK) plates and

incubated at 37 °C for 24 h to determine the number of survival cells. For the comparison, light control (bacterial cells and light without photocatalyst) and dark control (photocatalyst and bacterial cells without light) were also conducted in the study. The VL intensity during the photocatalysis was measured by a LI-250 light meter (LI-COR, Lincoln, USA) and was adjusted at an intensity of 8.0 $mW \cdot cm^{-2}$ for the experiments.

To identify the dominant reactive species (RS) accounting for the photocatalytic bacterial inactivation, specific compounds (i.e. respective RS scavengers) at predetermined optimized concentration were individually added into reaction solution with identical conditions mentioned above. All the above experiments were repeated in triplicates.

2.6 Prepare procedure for SEM observation of bacteria

The mixture of photocatalyst and *E. coli* K-12 before and after the inactivation were firstly sampled and centrifuged, and then the harvested cells were prefixed in 2.5% glutaraldehyde for 2 h and finally trapped in 0.1% (w/v) Poly-*L*-lysine. After washed with 0.1 M phosphate buffer solution, the specimens were dehydrated in a graded series of ethanol (50% for once, 70% for once, 85% for one time, 95% for two times, 100% for three times) each for 10 min. Finally, the cell samples were critical point dried and gold spur coated for SEM observation.

3. Results and discussion

3.1 Materials characterizations

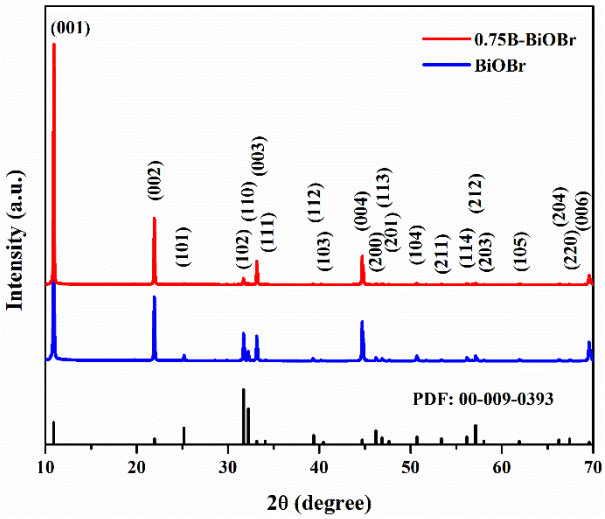

Figure 1 XRD patterns of B-BiOBr and BiOBr samples.

XRD patterns were carried out to investigate the changes of BiOBr crystal structure before and after B doping. As shown in Figure 1, all diffraction peaks can be well indexed as the tetragonal phase BiOBr (space group: *P4/nmm*, PDF 00-009-0393). The sharp XRD profile of {001} facet for both samples have a higher intensity than other diffraction peaks, indicating that the two samples have a preferred orientation along [001] zone axis. No diffraction peaks of B species are detected in the XRD pattern of 0.75B-BiOBr, which can be due to the low content of doping species. Additionally, no obvious peak shift is observed between two sets of patterns. Thus, the result suggests that introduction of B into BiOBr catalysts did not significantly change the crystal structure of as-prepared photocatalyst.

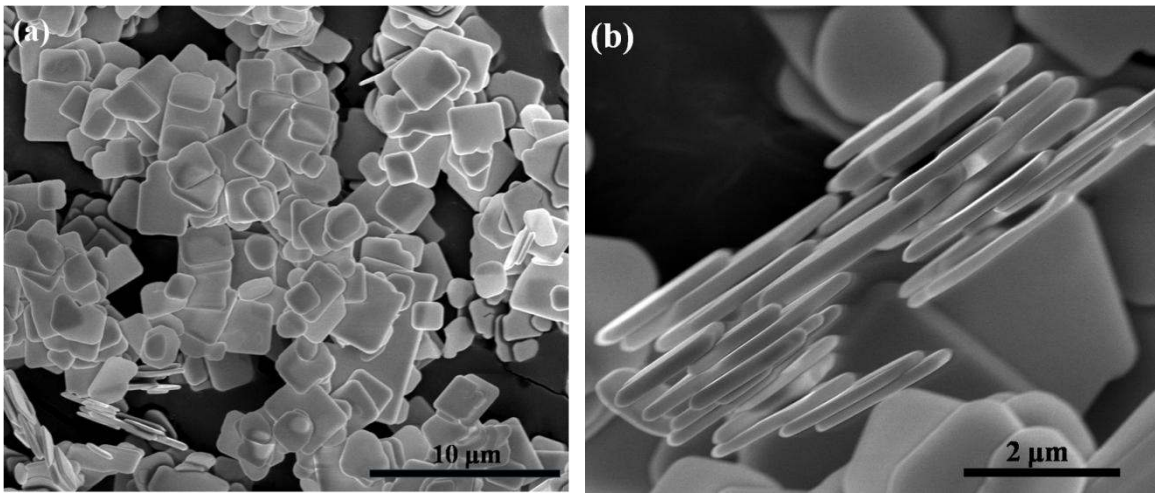

Figure 2 SEM images of 0.75B-BiOBr.

The morphology features of 0.75B-BiOBr are also observed through SEM images (Figure 2). The 0.75B-BiOBr sample is found to be square-like nanosheets with a diameter of 1.5-2.7 μm and a thickness of 150-300 nm. No significant difference is observed between the 0.75B-BiOBr and pure BiOBr (Figure S1), indicating that B doping also has negligible effect on the morphology of BiOBr samples. Particularly, the clear lattice fringes with an inter-planar lattice spacing of 0.278 nm and the angle of 90° (Figure S2) correspond to the (110) atomic planes. Moreover, the labeled angle in the corresponding fast Fourier transformation (FFT) pattern is about 45°, which is in a good agreement with the theoretical value of the angle between (110) and (200) planes. The spots from the FFT pattern can be indexed to the [001] direction, which is consistent with the XRD results. Based on the symmetries of tetragonal crystal structure of BiOBr, it can be concluded that the bottom and top surfaces of 0.75B-BiOBr nanosheets is the {001} facets, which is identical to that of pure BiOBr evidenced by our previous study [30]. Thus, this {001}-facet dominated feature is well preserved after B doping. Moreover, the area percentage of exposed {001}-facet for pure

BiOBr and 0.75B-BiOBr nanosheets is estimated both to be 86%. Therefore, the as-prepared 0.75B-BiOBr nanosheets still possess a high percentage of highly active {001} facets, which is expected to achieve enhanced VLD photocatalytic activities over pure BiOBr nanosheets in addition to the effect of doped B atoms.

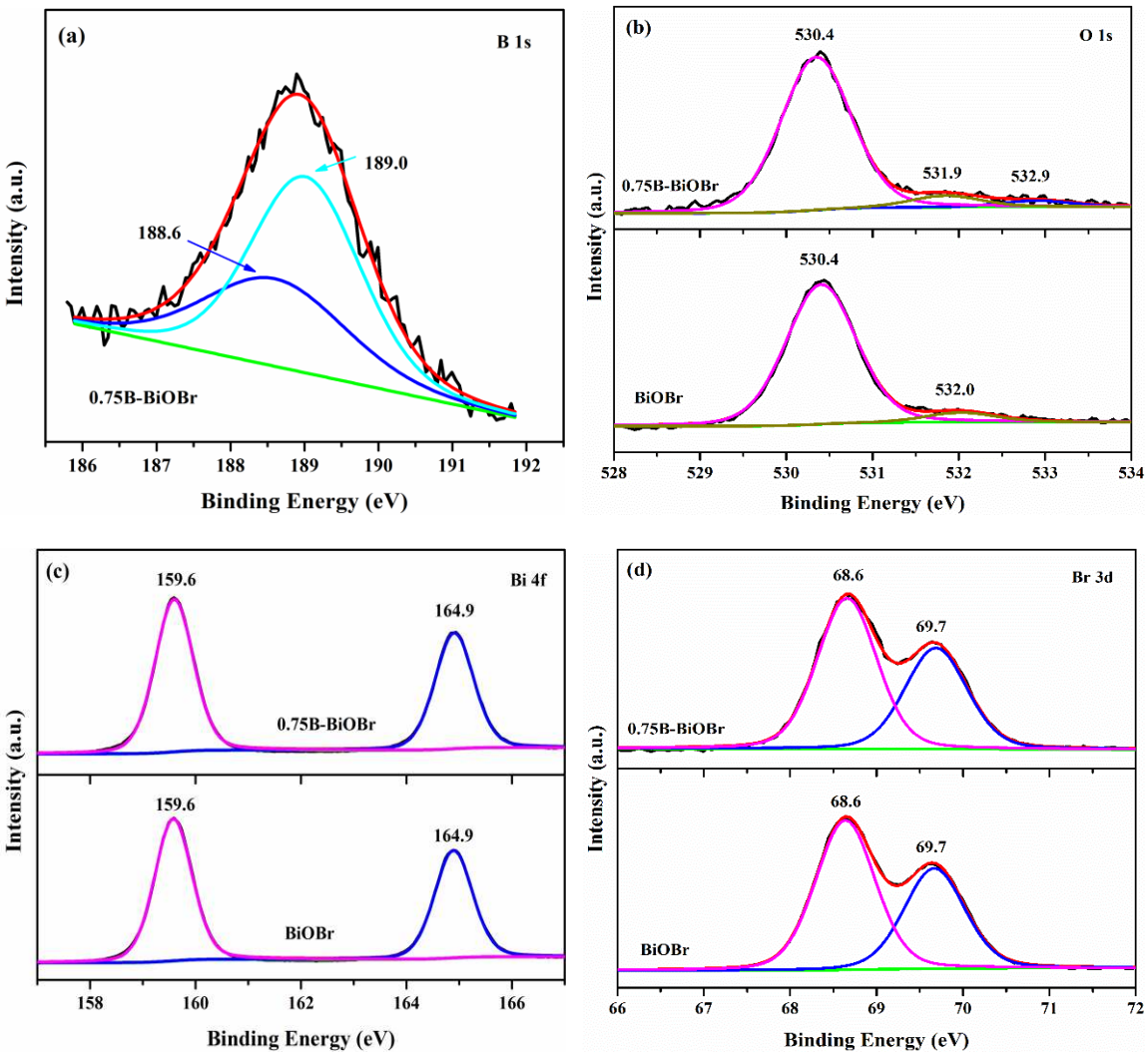

Figure 3 High resolution XPS spectra of (a) B 1s, (b) O 1s, (c) Bi 4f and (d) Br 3d of 0.75B-BiOBr and BiOBr nanosheets.

The distribution and chemical state of elements in the BiOBr nanosheets were

investigated with XPS spectra. Figure 3a shows the high-resolution XPS spectra of B 1s in B-BiOBr. Even if B is the most important element of interest, the B 1s spectrum could not be fully de-convoluted because it is overlapped with the peak of Br $3p_{1/2}$ (~189 eV). However, the B 1s spectral region shows a highly asymmetric profile, suggesting that at least one chemical valence state of B exists in the B-BiOBr sample in addition to Br $3p_{1/2}$. It is noteworthy that the binding energy (BE) of B 1s in B_2O_3 or H_3BO_3 is generally reported to be at about 194 eV [31]. The absence of these peaks verifies the absence of crystalline B_2O_3 and H_3BO_3 species in B-BiOBr samples, which also suggests that B have doped into the lattice of BiOBr rather than a simple physical mixture under hydrothermal treatment. The O1s spectrum of pure BiOBr nanosheets displayed in Figure 3b shows a broad asymmetrical peak, which can be de-convoluted into two peaks centered at 530.4 and 532.0 eV, respectively. They are attributed to crystal lattice O atoms (Bi-O) in BiOBr and surface hydroxyl group, respectively [32]. Besides the similar two peaks centered at 530.4 and 531.9 eV, an additional weak peak with BE of 532.9 eV was also observed after B doping, which could be associated with B–O bonds [33]. The above result confirms that B have doped into the BiOBr matrices. The shift of Bi-O bond exhibits no significant change because the electro-negativity of B (2.04) [34] is close to that of Bi (2.02) [35], thus leading negligible changes of the electron cloud density around O. The Bi 4f spectra (Figure 3c) show the symmetrical peaks at 159.58 and 164.8 eV which are attributed to Bi $f_{7/2}$ and Bi $f_{5/2}$ respectively. These results reveal that both the samples are comprised mainly of Bi^{3+}. The Br 3d peaks are associated with BE of 68.6 and 69.7 eV (Figure 3d), which is characteristic of Br^- in BiOBr materials. In comparison with the XPS spectra of Bi 4f and Br 3d, no obvious BE changes are found for two samples, which

demonstrates that doping B into the lattice of BiOBr cannot affect the electron density around Bi, as well as the interlayer van der Waals interaction in the crystal structure of BiOBr. BiOBr crystal is featured with a unique layered nanoarchitecture stacked by [Bi_2O_2] and Br layers (Figure S3). The distance between Bi−Bi ions and Bi−Cl ions in a single unit cell is 5.67, 3.09 (Bi−Br1) and 4.03 (Bi−Br2) Å, respectively [36, 37]. The distance of Bi−O and Bi−Bi in a [Bi_2O_2] unit is respectively 2.2 and 3.8 Å. Since these distance is much larger than the atomic radius of B (0.82 Å), it is possible that the B atoms dope into the [Bi_2O_2] unit or insert between the [Bi_2O_2] and Br layers. Based on the XPS results, some B–O bonds are formed, however, with no disturbance the chemical environment of Bi and Br. Therefore, it is highly speculated that the B atoms substitute the position of Bi or insert into the [Bi_2O_2] unit of BiOBr crystal. Unfortunately, it is hard to locate the accurate position of B atom in the crystal lattice of BiOBr at present, which deserves further in-depth investigation.

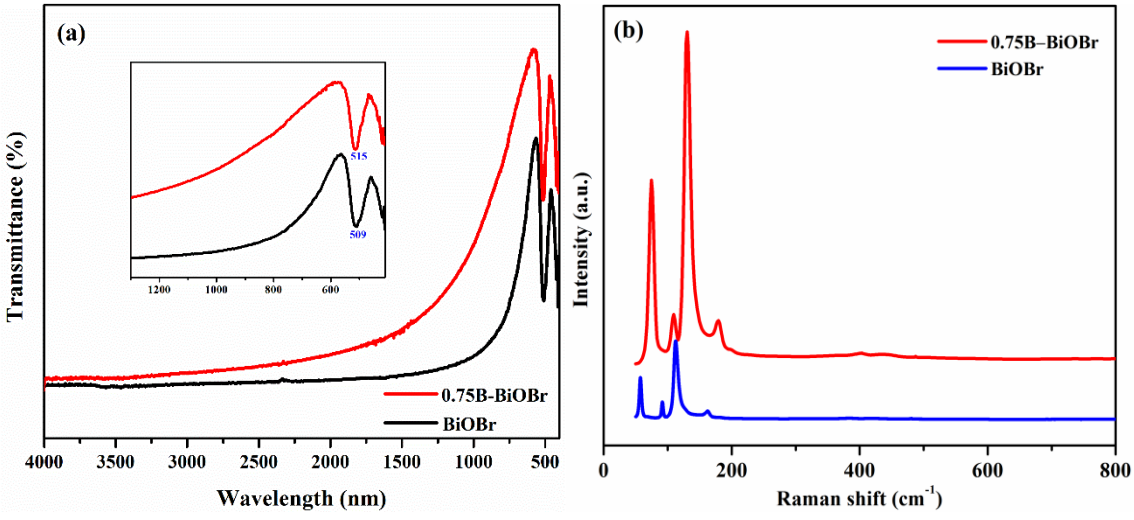

Figure 4 (a) FTIR spectra and (b) Raman spectra of 0.75B-BiOBr and BiOBr samples.

EDS analysis were also carried out to verify the existence of B element and elemental

distribution of B-BiOBr nanosheets. Figure S4 confirms the presence of Bi, O, Br and B elements in the B-BiOBr nanosheets. The evenly distributed B atoms provide direct evidence for the good dispersion of the B atoms in the lattice of BiOBr.

FTIR and Raman spectra are also employed to confirm the successful doping of B in BiOBr (Figure 4). For the FIIR spectrum of pure BiOBr in Figure 4a, 509 cm^{-1} is assigned to the Bi-O bond symmetric stretching vibration [32]. After doping with B, the stretching mode of Bi-O bond is found to be red-shifted about 6 cm^{-1} to 515 cm^{-1}. This suggests that the surrounding chemical environment affects the Bi-O bond vibration as B atoms are connected with O atoms, further validating the existence of B dopant in B-BiOBr nanosheets. Additionally, the absence of peak around 1200 cm^{-1} (the insert in Figure 4a) which belongs to B-O bonds in the B_2O_3 crystal [38], further excludes the existence of B_2O_3 after B doping in BiOBr nanosheets, in accordance with the results of XRD and XPS analyses. Figure 4b exhibits the Raman spectra of BiOBr nanosheets before and after B doping. For pure BiOBr sample, two bands at 57 and 91 cm^{-1} are ascribed to first-order vibration modes of Bi metal, while the band at 151 cm^{-1} is assigned to E_g internal Bi–Br stretching mode [39]. The strongest band at 112 cm^{-1} could be due to A_{1g} internal Bi–Br stretching mode. It is noted that B doping results in a significant red shift of these bands by *ca.* 18 cm^{-1} in comparison with pure BiOBr. What is more, despite of the weak E_g and B_{1g} bands at about 400 cm^{-1} generated by the motion of oxygen atoms for both samples, a unnoticeable hump appears for B-BiOBr nanosheets. Considering that the atomic radius of Bi (1.43–1.70 Å) is obviously larger than that of B (0.82 Å), the differences of Raman active modes between B-BiOBr and non-doped sample are attributed to the distortion of BiOBr crystal lattice induced by the doped B [40].

276

277 *3.2 Photocatalytic inactivation of bacteria*

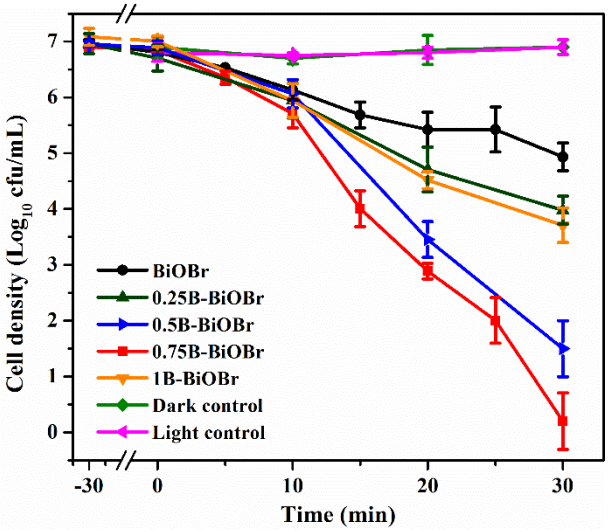

278

279 **Figure 5** Photocatalytic inactivation of *E. coli* K-12 by BiOBr and B-BiOBr photocatalysts

280 under VL irradiation.

281

282 A common waterborne bacterium, *E. coli* K-12, was chosen as a model bacterium to

283 evaluate the photocatalytic inactivation activity of B-BiOBr nanosheets. In the control

284 experiments, the bacterial population keeps unchanged within 30 min, indicating no toxic

285 effects of pure BiOBr and B-BiOBr photocatalysts on bacterial cells (Figure S5) and no

286 photolysis of *E. coli* K-12 cells (Figure 5) under VL irradiation. When employing B-BiOBr

287 nanosheets as photocatalysts, they exhibit excellent photocatalytic performance to inactivate

288 *E. coli* K-12 cells. The inactivation efficiency increases with increasing the content of B

289 dopant. The 0.75B-BiOBr nanosheet shows the best bacterial inactivation activity, with 10^7

290 (i.e. 7-log) bacterial cells being completely inactivated within 30 min under VL irradiation.

291 However, further increasing the doping content (1B-BiOBr) leads to the significant decrease

292 of the inactivation efficiency. This is because the excess B will serve as a trap center for

recombination of charge carriers to overcome the advantages their separation. In contrast, only 5-log reduction of cell density is observed within 30 min irradiation for pure BiOBr nanosheets, which is much slower than that of B-BiOBr nanosheets, indicating that the B dopant can remarkably enhance the photocatalytic bacterial inactivation efficiency of BiOBr nanosheets. Moreover, recycling experiments were carried out to investigate the stability and reusability of the photocatalyst in bacterial inactivation. As shown in Figure S6a, no noticeable reduction of bacterial inactivation efficiency is observed after 3 cycles. Additionally, the photocatalyst still possesses nanosheet-like morphology without obvious changes after each run (Figures 6b-d), suggesting that the 0.75B-BiOBr photocatalyst is stable during the photocatalytic bacterial inactivation process.

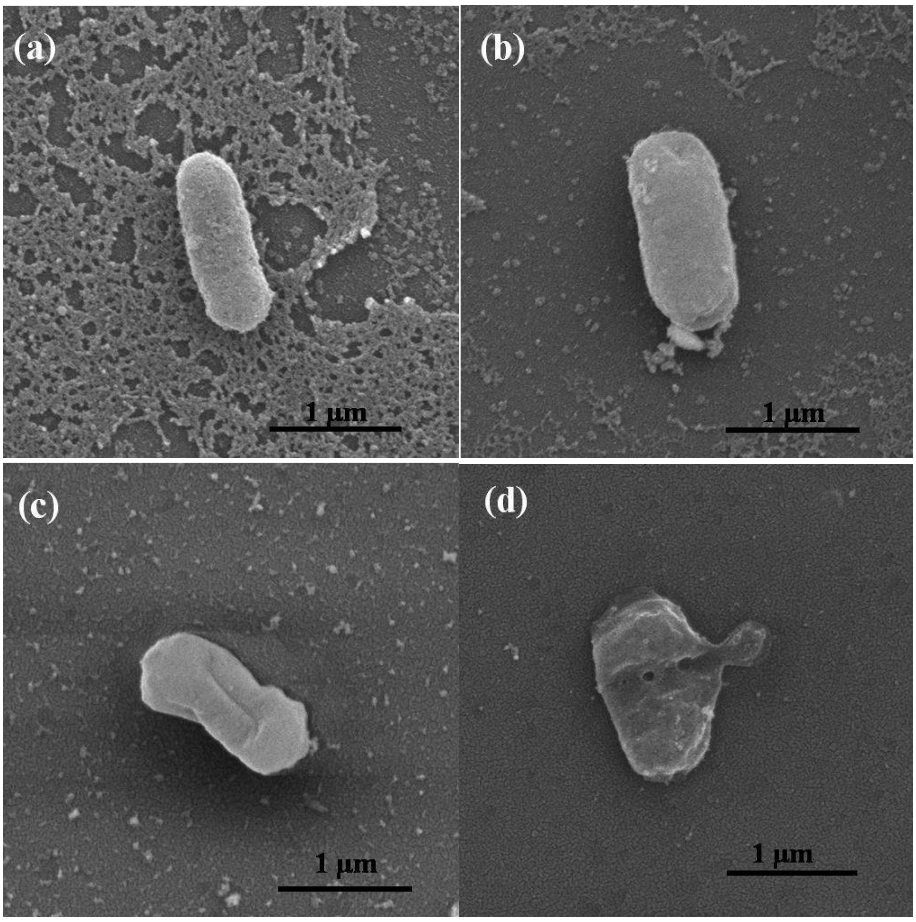

Figure 6 SEM images of individual *E. coli* K-12 cell being photocatalytically inactivated by 0.75B-BiOBr for (a) 0 h, (b) 2 h, (c) 6 h and (d) 12 h.

In order to understand the destruction process of bacterial cells photocatalyzed by 0.75B-BiOBr nanosheets, SEM observation was conducted to examine the morphology changes during the photocatalytic inactivation process (Figure 6). Prior to the photocatalytic inactivation, *E. coli* K-12 exhibits a well-preserved rod shape and intact cell structure (Figure 6a). After 2 h photocatalytic treatment, the bacteria cell shows a rough surface with the formation of pits in their cell wall (Figure 6b), suggesting initial damage to the outer membrane and a following leakage of the interior contents. Prolonging the inactivation time to 6 h, the shape of bacterial cell becomes depressed and abnormal (Figure 6c), indicating more severe damage and increased cell permeability. Finally, disorganized membrane structures is observed after 12 h irradiation (Figure 6d), which demonstrates that the cell is completely decomposed. This observation suggests that the destruction process of the bacterial cell is progressive from the cell membrane to the inner cellular components, leading to the final collapses of bacterial cells. This matches well with the previous studies that photocatalytic treatment can induce significant disorder in membrane permeability of bacterial cells [41, 42]. Furthermore, from the corresponding enlarged SEM images in Figure S7, there is no noticeable morphology changes during the photocatalytic inactivation process, further confirming the photostability of 0.7B-BiOBr photocatalyst.

The bacterial cell membrane provides a permeability barrier to the passage of small ions. Hence, the leakage of potassium ion (K^+), which is a critical intracellular cation in bacteria,

was examined as an indicator of membrane permeability changes [43]. As expected, the photocatalytic process immediately causes the leakage of K^+, which increases promptly up to nearly 1000 ppb and becomes steady beyond that (Figure S8). Comparatively, no significant leakage of K^+ is observed in the control experiments. Therefore, the role of 0.75B-BiOBr photocatalyst to cause the membrane damage and leakage appears very prominent, in paralleled to the loss of cell viability with increasing irradiation time.

3.3 Photocatalytic mechanisms

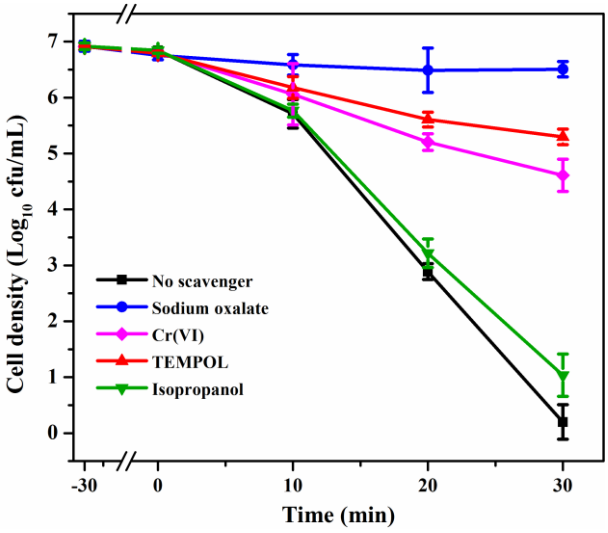

Figure 7 Photocatalytic inactivation efficiencies with respective RSs scavengers (sodium oxalate, 0.5 mM; Cr(VI), 0.05 mM; Fe-EDTA, 0.1 mM; TEMPOL, 2 mM; isopropanol, 0.5 mM) in the presence of 0.75B-BiOBr nanosheets.

The scavengers study was carried out to understand the contributions of various RSs during the photocatalytic inactivation process catalyzed by 0.75B-BiOBr. Before conducting the experiments, the concentrations used for each compound are optimized to ensure their maximum scavenging effect but would not cause any toxicity to the bacterial cells.

345 Significantly, the chosen concentration of toxic Cr(VI) has no toxicity towards bacteria cells
346 (Figure S9). As shown in Figure 7, the bacterial inactivation is virtually suppressed with the
347 addition of sodium oxalate as the scavenger of hole (h^+), suggesting that h^+ played a major
348 role in the photocatalytic inactivation process. It is not surprising that the inactivation
349 efficiency was significantly inhibited after adding Cr(VI) to capture electron (e^-) in the
350 system, due to the enhanced hole-electron separation efficiency by consumption of e^- and
351 thermodynamically favorable inactivation process mediated by h^+ concomitantly. Similarly,
352 the importance of superoxide ($\bullet O_2^-$) was affirmed by the great decrease in the inactivation
353 efficiency after adding TEMPOL as a scavenger. However, after adding isopropanol to quench
354 hydroxyl radical (•OH), no significant change in the inactivation efficiency was observed as
355 compared with that without scavengers added, implying the minor or no contribution of •OH
356 in the inactivation process. The minor role of •OH is expected, because the generation of •OH
357 is thermodynamically forbidden from h^+ due to the more negative redox potential of
358 Bi(V)/Bi(III) (+1.59 eV) than that of $\bullet OH/OH^-$ (+1.99 eV) and $\bullet OH/H_2O$ (+2.73 eV) [10]. In
359 brief, these results demonstrate that h^+ was the major reactive species accounting for the
360 inactivation process in the present photocatalytic system.

361 To provide more solid evidence to verify the major contribution of h^+, reactive species of
362 $\bullet O_2^-$, •OH and H_2O_2 generated in the B-BiOBr and BiOBr systems were quantitatively
363 compared. NBT and TA were applied as the specified probe for $\bullet O_2^-$ and •OH, respectively.
364 As shown in Figure 8a, just a slightly higher concentrations of $\bullet O_2^-$ are detected within 30
365 min VL irradiation in 0.75B-BiOBr system compared with pure BiOBr system. No
366 measurable •OH are observed in both the bacterial inactivation processes (Figure 8b),

corresponding to the results of scavenger studies. Likewise, the difference of derived H_2O_2 can also be ignored (Figure 8c). The short-lived radicals of $\bullet O_2^-$ and •OH were also evidenced by EPR measurements using

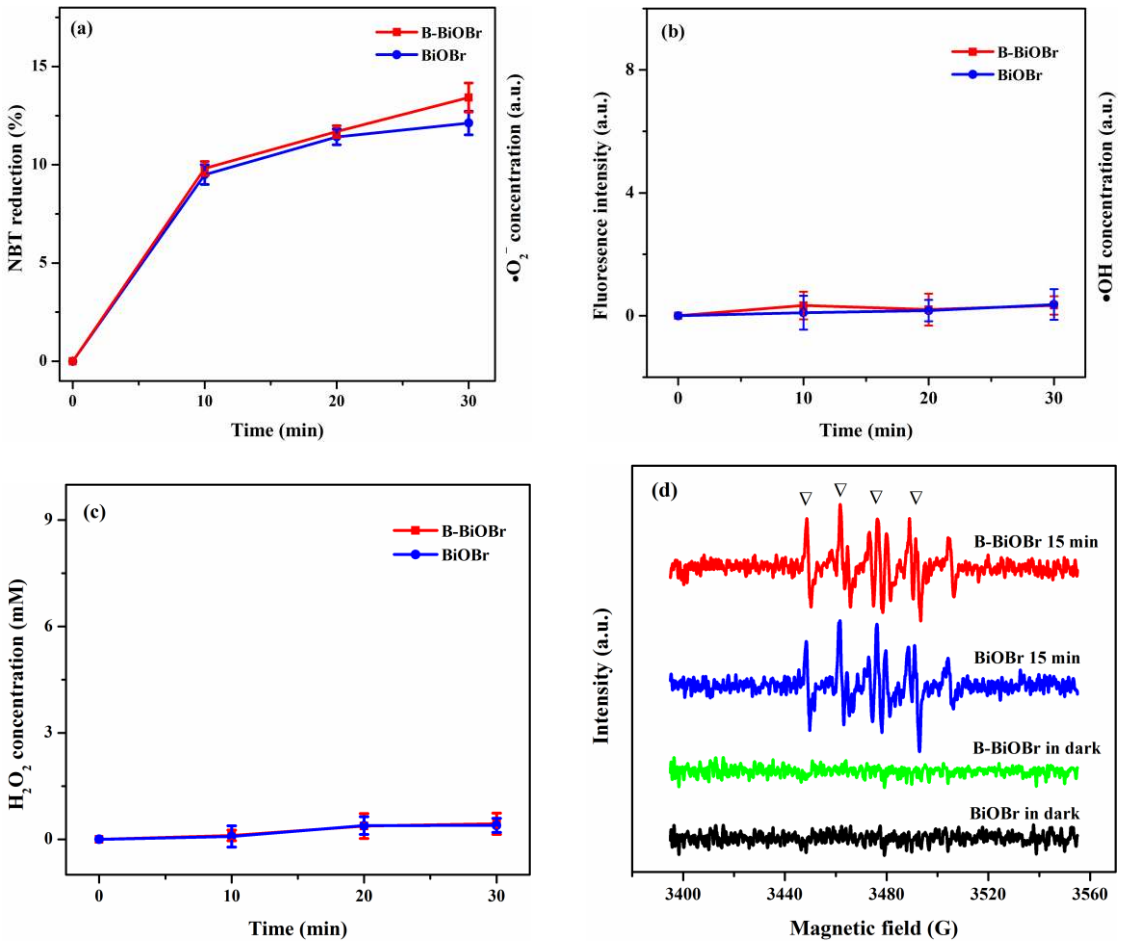

Figure 8 Relative concentration of (a) $\bullet O_2^-$, (b) •OH, (c) H_2O_2 and (d) EPR spectra of DMPO-$\bullet O_2^-$ in the presence of 0.75B-BiOBr and pure BiOBr nanosheets under VL irradiation.

5,5-dimethyl-1-pyrroline N-oxide (DMPO) as a spin-trap. As shown in Figure 8d, no resonance signal is detected for the two samples in dark. After VL illumination, the characteristic signal of the DMPO-$\bullet O_2^-$ spin adduct was presented, affirming the generation of $\bullet O_2^-$ for B-BiOBr and BiOBr samples. Furthermore, the intensity of the two signals is similar

to each other, implying that there is no considerate enhancement of photogenerated $\bullet O_2^-$ for B-BiOBr sample, which corresponds to the result of NBT measurement. Moreover, no obvious signals of DMPO-•OH spin product are detected, which corresponds to the result of TA measurement. Consequently, B-BiOBr nanosheet photocatalyst has no obvious effect on the amount of photogenerated RSs of $\bullet O_2^-$, •OH and H_2O_2. Overall, these findings justify the dominant contribution of h^+ for the superior photocatalytic inactivation activity of B-BiOBr nanosheets over BiOBr photocatalysts.

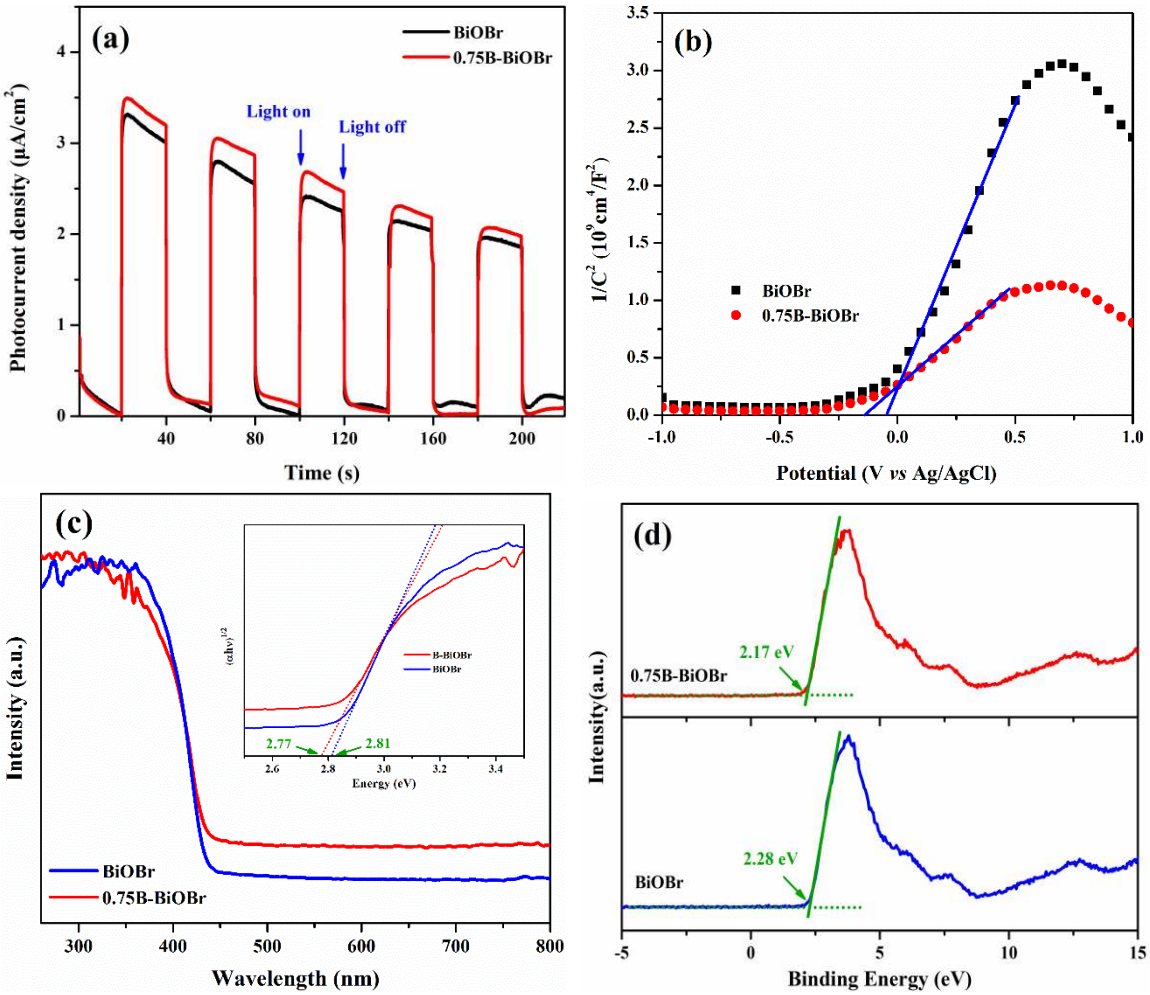

Figure 9 (a) Transient photocurrent response under VL irradiation and (b) Mott–Schottky plots (Na_2SO_4: 0.1 M) (c) UV-vis diffuse reflectance spectra, (d) valence band XPS spectra of

0.75B-BiOBr and BiOBr samples.

Electrochemical experiments were carried out to in-depth investigate the h^+ mediated photocatalytic inactivation enhancement of B doping BiOBr photocatalysts. Figure 9a shows the transient photocurrent responses of pure BiOBr and 0.75B-BiOBr nanosheets over multiple on/off cycles under intermittent VL irradiation. The higher photocurrent response is observed for 0.75B-BiOBr, revealing more efficient photoexcited e^-/h^+ separation over 0.75B-BiOBr compared to pure BiOBr. Figure S10 shows the electrochemical impedance spectroscopy (EIS) presented as Nyquist plots in the absence and in the presence of VL irradiation. The impedance arc radius of 0.75B-BiOBr is found to be smaller than that of BiOBr both in dark and under VL irradiation, which signifies a more effective separation and faster interfacial transfer of photogenerated e^-/h^+ pairs. The Mott-Schottky plots were presented in Figure 9b. The positive slope of the plots is consistent with the typical behavior of n-type semiconductors. The flat band potential (V_{fb}), which is calculated from the *x* intercepts of the linear region, is estimated to be −0.05 and −0.14 V (*vs* Ag/AgCl) for pure BiOBr and 0.75B-BiOBr, respectively. Generally, the measured flat band potential equals to the Fermi level (E_f) for an n-type semiconductor [44]. Thus, a more negative shift of E_f indicates a higher conduction band position of 0.75B-BiOBr compared with pure BiOBr. Furthermore, the 0.75B-BiOBr nanosheets exhibit a smaller slope of the Mott–Schottky plot than the pure one, inferring an increased donor density. The carrier density was calculated from the slope of Mott–Schottky plots, which can be simplified as following equation:

$$\frac{1}{C^2} = \left(\frac{2}{e\mathrm{N_d}\varepsilon_0\varepsilon} \right) |V - V_{\mathrm{fb}}|$$

where C is the space charge capacitance, *e* is the electronic charge, ε is the dielectric constant of BiOBr; ε_0 is the permittivity of free space, N_d is the carrier density; *V* is the applied potential. Accordingly, the calculated carrier density is 2.9×10^{-19} and 7.1×10^{-19} cm^{-3} for pure BiOBr and 0.75B-BiOBr, respectively. Therefore, the B doping can increase the carrier density of BiOBr. The UV-Vis DRS spectra in Figure 9c show some extension of absorption edge to VL region by the introduction of B atoms. The red-shift of the absorption edge is mainly attributed to the doped B in the BiOBr matrix [45]. Since the absorption ability of VL for B-BiOBr is strengthened, the B doping can provide the prerequisites for the improvement of photocatalytic invitation. The energy band gap (E_g) of semiconductors can be estimated by using the equation $(\alpha h\nu) = A(h\nu - E_g)^n$, where α is the absorption coefficient, hν is the photo energy, and n = 2 for BiOBr as an indirect semiconductor. The calculated E_g of B-BiOBr (2.77 eV) was a little smaller than the pure BiOBr (2.81 eV), indicating B doping can decrease the band gap energy of BiOBr. In order to understand the underlying intrinsic inactivation mechanism in depth, it is also vital to locate the positions of the valence band maximum (VBM) and conduction band minimum (CBM) of B-BiOBr. Figure 9d presents the valence band XPS spectra of B-BiOBr and BiOBr samples. The overlapping absorption edges of two samples suggest that the intrinsic bandgap is independent of the chemical states of B. Similar phenomena can be also found that doped B leads to no changes in the intrinsic bandgap of TiO_2 [46]. However, the VBM of 0.75B-BiOBr is slightly shifted upwards by 0.11 eV from 2.28 eV to 2.17 eV with respect to BiOBr. Concomitantly, the CBM of B-BiOBr up-shifts by 0.07 eV and occurs at − 0.6 eV compared with that of pure BiOBr (− 0.53 eV), according to

the optical adsorption spectra, which is in a good agreement with the result of Mott–Schottky plot. The VB width and CBM energy are the two important features worthy to note from the viewpoint of kinetic and thermodynamic requirements for the photocatalytic reactions [47]. As the VB width intrinsically governs the mobility of photoexcited h^+, the wider CB width leads to the better oxidation ability of h^+ attributing to their higher mobility. On the other hand, the elevation of the CBM results in higher charges separation by promoting the transfer of photogenerated electrons, which is consistent with the result of higher carrier density and photocurrent of B-BiOBr sample.

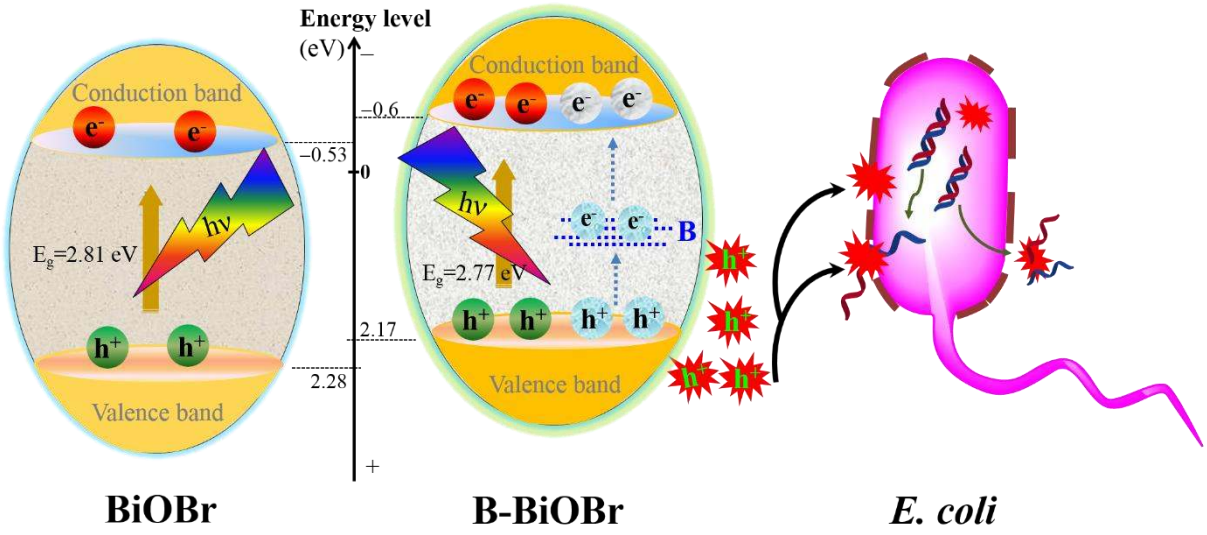

Figure 10 Proposed photocatalytic bacterial inactivation enhancement of B-BiOBr nanosheets.

Our previous study emphasized that h^+ and $\bullet O_2^-$ make the major contributions to the inactivation process of pure BiOBr [30]. Since no considerate enhancement of photogenerated $\bullet O_2^-$ yield, the photoexcited h^+ should be responsible for the superior inactivation

449 performance of B-BiOBr over pure BiOBr. Accordingly, the h^+ meditated mechanism for the
450 photocatalytic bacterial enhancement of B-BiOBr is proposed, as illustrated in Figure 10. On
451 one hand, e^- are photoexcited to CB of BiOBr, leaving h^+ in its VB. On the other hand, B is
452 configured with not filled and contain unpaired electrons, making it as good e^- acceptors [48].
453 Owing to the electron-deficient character of B, it is easy for B to promote an extra e^- from VB
454 and subsequently excited to the CB of BiOBr. Simultaneously, an extra h^+ is left in VB of
455 BiOBr. Thus, B could enhance the e^-/h^+ pair separation efficiency of BiOBr. Consequently,
456 owing to the raised CB, higher amount of h^+ with higher oxidative ability is generated for
457 B-BiOBr nanosheets compared with pure BiOBr. In brief, with predominate role over the $\bullet O_2^-$
458 derived from e^- of CB, the photogenerated h^+ could be functioned to directly oxidize bacterial
459 cells, from the cell membrane to the released intracellular substrates, resulting in superior
460 photocatalytic inactivation activity of B-BiOBr over pure BiOBr nanosheets.
461

462 ## 4. Conclusion

463 VLD B-BiOBr nanosheets photocatalysts was prepared via a simple hydrothermal method. It
464 was found that B atoms are successfully doped into the crystal lattice of BiOBr. Significantly,
465 the as-prepared B-BiOBr nanosheets show superior activity in the photocatalytic inactivation
466 of a typical bacterium, *E. coli* K-12, over pure BiOBr nanosheets under VL irradiation. The
467 destruction process of bacterial cell by this newly prepared photocatalyst is also monitored
468 from the attack of cell membrane to the release of intracellular components. Photogenerated
469 h^+ is evidenced as the major RS responsible for the bacterial inactivation process in the
470 B-BiOBr-VL photocatalytic system. The enhanced photocatalytic bacterial inactivation is

mainly originated from the doped B, which facilitates the photoexcited e^-/h^+ pair separation efficiency of B-BiOBr nanosheets.

Acknowledgement

The research was supported by ITSP Tier 3 Scheme (ITS/216/14) of Innovation & Technology Commission and Research Grant Council of Hong Kong SAR Government (GRF14100115), National Natural Science Funds for Distinguished Young Scholars (41425015) and National Science Foundation of China (21077104). P.K. Wong was also supported by the CAS/SAFEA International Partnership Program for Creative Research Teams of Chinese Academy of Sciences, China. The authors would also like to acknowledge the technical support provided by Analytical and Testing Center, Huazhong University of Science and Technology, China.

References

[1] W.J. Ong, S.Y. Voon, L.L. Tan, B.T. Goh, S.T. Yong, S.P. Chai, Ind. Eng. Chem. Res. 53 (2014) 17333-17344.

[2] D. Wu, W. Wang, T.W. Ng, G. Huang, D. Xia, H.Y. Yip, H.K. Lee, G. Li, T. An, P.K. Wong, J. Mater. Chem. A 4 (2016) 1052-1059.

[3] L.L. Tan, W.J. Ong, S.P. Chai, B.T. Goh, A.R. Mohamed, Appl. Catal. B: Environ. 179 (2015) 160-170.

[4] W.J. Ong, L.L. Tan, S.P. Chai, S.T. Yong, A.R. Mohamed, Nano Energy 13 (2015) 757-770.

493 [5] H. Sun, S. Liu, S. Liu, S. Wang, Appl. Catal. B: Environ. 146 (2014) 162-168.

494 [6] X. Chen, A. Selloni, Chem. Rev. 114 (2014) 9281-9282.

495 [7] W.J. Ong, L.L. Tan, S.P. Chai, S.T. Yong, A.R. Mohamed, Nano Res. 7 (2014)
496 1528-1547.

497 [8] X.Q. Wang, W.X. Liu, J. Tian, Z.H. Zhao, P. Hao, X.L. Kang, Y.H. Sang, H. Liu, J. Mater.
498 Chem. A 2 (2014) 2599-2608.

499 [9] H.B. Hou, X.X. Wang, C.C. Chen, D.M. Johnson, Y.F. Fang, Y.P. Huang, Catal. Commun.
500 48 (2014) 65-68.

501 [10] H. Cheng, B. Huang, Y. Dai, Nanoscale 6 (2014) 2009-2026.

502 [11] Z. Ai, W. Ho, S. Lee, J.Phys. Chem. C 115 (2011) 25330-25337.

503 [12] J. Di, J. Xia, Y. Ge, L. Xu, H. Xu, J. Chen, M. He, H. Li, Dalton Trans. 43 (2014)
504 15429-15438.

505 [13] J. Xia, J. Di, H. Li, H. Xu, H. Li, S. Guo, Appl. Catal. B: Environ. 181 (2016) 260-269.

506 [14] G. Jiang, X. Wang, Z. Wei, X. Li, X. Xi, R. Hu, B. Tang, R. Wang, S. Wang, T. Wang, J.
507 Mater. Chem. A 1 (2013) 2406-2410.

508 [15] Z. Liu, B. Wu, Y. Zhao, J. Niu, Y. Zhu, Ceram. Int. 40 (2014) 5597-5603.

509 [16] Z. Wei, G. Jiang, L. Shen, X. Li, X. Wang, W. Chen, MRS Commun. 3 (2013) 145-149.

510 [17] G. Jiang, R. Wang, X. Wang, X. Xi, R. Hu, Y. Zhou, S. Wang, T. Wang, W. Chen, ACS
511 Appl. Mater. Interfaces 4 (2012) 4440-4444.

512 [18] H. Lin, X. Li, J. Cao, S. Chen, Y. Chen, Catal. Commun. 49 (2014) 87-91.

513 [19] G. Jiang, X. Li, Z. Wei, X. Wang, T. Jiang, X. Du, W. Chen, Powder Technol. 261 (2014)
514 170-175.

515 [20] S. Wang, E. Iyyamperumal, A. Roy, Y. Xue, D. Yu, L. Dai, Angew. Chem. Int. Ed. 50
516 (2011) 11756-11760.
517 [21] M. Sathish, B. Viswanathan, R. Viswanath, Appl. Catal. B: Environ. 74 (2007) 307-312.
518 [22] G. Liu, L.C. Yin, P. Niu, W. Jiao, H.M. Cheng, Angew. Chem. 125 (2013) 6362-6365.
519 [23] N. Lu, X. Quan, J. Li, S. Chen, H. Yu, G. Chen, J. Phys. Chem. C 111 (2007)
520 11836-11842.
521 [24] T.S. Hansen, J. Mielby, A. Riisager, Green Chem. 13 (2011) 109-114.
522 [25] H.J. Zhai, B. Kiran, J. Li, L.S. Wang, Nature Mater. 2 (2003) 827-833.
523 [26] X. Wang, Z. Zeng, H. Ahn, G. Wang, Appl. Phys. Lett. 95 (2009) 183103.
524 [27] D. Quiñones, A. Rey, P. Álvarez, F. Beltrán, G.L. Puma, Appl. Catal. B: Environ. (2014).
525 [28] Y. Fu, C. Chang, P. Chen, X. Chu, L. Zhu, J. Hazard. Mater. 254 (2013) 185-192.
526 [29] L.W. Shan, G.L. Wang, J. Suriyaprakash, D. Li, L.Z. Liu, L.M. Dong, J. Alloys Compd.
527 636 (2015) 131-137.
528 [30] D. Wu, B. Wang, W. Wang, T.C. An, G.Y. Li, T.W. Ng, H.Y. Yip, C.M. Xiong, H.K. Lee,
529 P.K. Wong, J. Mater. Chem. A 3 (2015) 15148-15155.
530 [31] M. Wang, Y. Che, C. Niu, M. Dang, D. Dong, J. Hazard. Mater. 262 (2013) 447-455.
531 [32] L. Ye, J. Liu, Z. Jiang, T. Peng, L. Zan, Appl. Catal. B: Environ. 142 (2013) 1-7.
532 [33] T.T. Wu, Y.P. Xie, L.C. Yin, G. Liu, H.M. Cheng, J.Phys. Chem. C 119 (2015) 84-89.
533 [34] T.P. Kaloni, Y. Cheng, U. Schwingenschlögl, J. Mater. Chem. 22 (2012) 919-922.
534 [35]S. Liu, H. Zhang, L. Sviridov, L. Huang, X. Liu, J. Samson, D. Akins, J. Li, S. O'Brien, J.
535 Mater. Chem. 22 (2012) 21862-21870.
536 [36] A. Dash, S. Sarkar, V.N.K.B. Adusumalli, V. Mahalingam, Langmuir 30 (2014)

537 1401-1409.
538 [37] L.J. Zhao, X.C. Zhang, C.M. Fan, Z.H. Liang, P.D. Han, Physica B 407 (2012)
539 3364-3370.
540 [38] X. Xue, Y. Wang, H. Yang, Appl. Surf. Sci. 264 (2013) 94-99.
541 [39] K. Zhao, L. Zhang, J. Wang, Q. Li, W. He, J.J. Yin, J. Am. Chem. Soc. 135 (2013)
542 15750-15753.
543 [40]Y. Dong, C. Feng, J. Zhang, P. Jiang, G. Wang, X. Wu, H. Miao, Chem. Asian J. 10 (2015)
544 687-693.
545 [41] G. Huang, D. Xia, T. An, T.W. Ng, H.Y. Yip, G. Li, H. Zhao, P.K. Wong, Appl. Environ.
546 Microbiol. (2015) 00775-00715.
547 [42] L.S. Zhang, K.H. Wong, H.Y. Yip, C. Hu, J.C. Yu, C.Y. Chan, P.K. Wong, Environ. Sci.
548 Technol. 44 (2010) 1392-1398.
549 [43] S. Swetha, M. Kumari Singh, K. Minchitha, R. Geetha Balakrishna, Photochem.
550 Photobiol. 88 (2012) 414-422.
551 [44] X.Q. An, X.L. Yu, J.C. Yu, G.J. Zhang, J. Mater. Chem. A 1 (2013) 5158-5164.
552 [45] K. Yang, Y. Dai, B. Huang, Phys. Rev. B 76 (2007) 195201.
553 [46] G. Liu, J. Pan, L. Yin, J.T. Irvine, F. Li, J. Tan, P. Wormald, H.M. Cheng, Adv. Funct.
554 Mater. 22 (2012) 3233-3238.
555 [47] M. Guan, C. Xiao, J. Zhang, S. Fan, R. An, Q. Cheng, J. Xie, M. Zhou, B. Ye, Y. Xie, J.
556 Am. Chem. Soc. 135 (2013) 10411-10417.
557 [48] M.V. Dozzi, E. Selli, J. Photochem. Photobiol. C 14 (2013) 13-28.

*Graphical Abstract

TOC